ACS APPLIED BIO MATERIALS

Article

CT/MR Dual-Modal Imaging Tracking of Mesenchymal Stem Cells Labeled with Au/GdNC@SiO2 Nanotracer in Pulmonary Fibrosis

Jie Huang, Jie Huang, Hongying Bao, Xinyu Ning,
Chenggong Yu, Zhongjin Chen, Jie Chao, and Zhijun Zhang

ACS Appl. Bio Mater., **Just Accepted Manuscript** • DOI: 10.1021/acsabm.0c00195 • Publication Date (Web): 11 Mar 2020

CT/MR Dual-Modal Imaging Tracking of Mesenchymal Stem Cells Labeled with Au/GdNC@SiO_2 Nanotracer in Pulmonary Fibrosis

Jie Huang,† Jie (Holly) Huang,‡ Hongying Bao,† Xinyu Ning,† Chenggong Yu,† Zhongjin Chen,† Jie Chao,*‡ and Zhijun Zhang*†

† CAS Key Laboratory of Nano-Bio Interface, Division of Nanobiomedicine, Suzhou Institute of Nano-Tech and Nano-Bionics, Chinese Academy of Sciences, Suzhou 215123, Jiangsu, China.

‡ Department of Physiology, School of Medicine, Southeast University, Nanjing 210009, Jiangsu, China.

ABSTRACT: Mesenchymal stem cells (MSCs) have shown potential as an innovative treatment for pulmonary fibrosis (PF), due to their capability of amelioration of inflammation and moderation of deterioration of PF. The fate of the stem cells transplanted into lung, including survival, migration, homing, and functions, however, has not been fully understood yet. In this paper, we report the development of a CT/MR dual-modal nanotracer, gold/gadolinium nanoclusters overcoated with a silica shell (Au/GdNC@SiO_2), for noninvasive labeling and tracking of the transplanted human MSCs (hMSCs) in PF model. The Au/GdNC@SiO_2 nanotracer exhibits good colloidal and chemical stability, high biocompatibility, enhanced longitudinal MR relaxivity, and superior X-ray attenuation property. And the hMSCs can be labeled by Au/GdNC@SiO_2 effectively, resulting in significantly increased cellular CT/MR imaging contrast, without any obvious adverse effect on the function, including proliferation and differentiation of the labeled stem cells. Moreover, by using the Au/GdNC@SiO_2 nanotracer, the hMSCs transplanted in lung can be tracked for 7 d via *in vivo* CT/MR dual modality imaging. This work may provide an insight into the role the transplanted hMSCs play in PF therapy, and therefore promoting the stem cell-based regenerative medicine.

KEYWORDS: idiopathic pulmonary fibrosis; mesenchymal stem cell; Au/Gd nanotracer; CT/MR dual-modal imaging; *in vivo* tracking

1. INTRODUCTION

Pulmonary fibrosis (PF) is one of the most serious diseases of the respiratory system with a high mortality rate, however, the optimal method for PF treatment is not established.[1, 2] Previous studies revealed that mesenchymal stem cells (MSCs) derived from adult tissues could directly target the lung lesions, secrete therapeutic factors and participate in the lung tissue regeneration.[3-5] These studies implied that MSCs-based therapy may be developed for the effective intervention of lung diseases. However, the MSCs-based lung disease therapy is still in the early stage of development due to the lack of a profound and thorough understanding of the fate, such as distribution, migration, survival, and functions, of the transplanted hMSCs.[6, 7] Histological examination is a widely used method for obtaining the above information. However, such a method is invasive and time-consuming. Therefore, the development of advanced imaging techniques that provide noninvasive, reproducible, and synchronous tracking of the cells after transplantation *in vivo* is highly desired.

In recent years, a variety of biomedical imaging techniques, such as positron emission tomography (PET),[8] single photon emission computed tomography (SPECT),[9] magnetic resonance imaging (MRI),[10] magnetic particle imaging (MPI),[11, 12] computed tomography (CT) imaging,[13] fluorescence imaging,[14, 15] bioluminescence,[16, 17] and multispectral optoacoustic tomography,[18, 19] to name a few, have been extensively exploited to track the transplanted stem cells noninvasively. Among these imaging techniques, CT and MRI are two most commonly used imaging tools in clinic. CT imaging has high spatial resolution and can quantify the cells.

However, its detection sensitivity is very low. The use of CT contrast agents with efficient X-ray attenuation properties could help, but the soft-tissue image contrast is still very low.[20-22] On the contrary, MRI has high detection sensitivity and soft-tissue contrast. To track the stem cells with MRI technique, the cells are usually labeled by magnetic tracers, including iron oxide nanoparticles and gadolinium-based contrast agents.[23, 24] However, the low proton density of lung tissue influences the signal intensity of MRI. Therefore, either CT imaging or MRI alone is insufficient to obtain all the necessary information of the transplanted cells. The development of a multifunctional platform that integrates CT and MR imaging modalities can overcome the inherent shortcomings of each modality in the tracing of the hMSCs transplanted in lung.

Many types of nanomaterials that combine CT and MR imaging techniques for tumor detection have been developed.[25, 26] However, in the design of nanotracers for MSCs tracking, several criteria should be taking into consideration. First, the nanotracers should be biocompatible and not interfere with the cell functions, including cell viability, migration, and differentiation of the labeled MSCs. Second, the nanotracers must maintain their physiochemical stability inside the labeled cells. Third, the nanotracers should possess high cell labeling efficiency and imaging contrast to allow detecting and monitoring of the transplanted cells *in vivo*.[27] Last, the nanotracers should possess long-period *in vivo* cell tracking performance. It takes periods spanning several weeks for stem cells to exhibit their treatment efficacy, so the nanotracers are required to trace the transplanted MSCs in quite a long period.[12] Gold nanomaterials are ideal

CT nanotracers for MSCs tracking due to their strong X-ray absorption coefficient (5.16 cm^2 g^{-1} at 100 keV), good colloidal stability and biocompatibility, sustained contrast, shape and size controllability, surface modifiability, and little adverse effects on the labeled MSCs.[13, 28-30] Furthermore, gadolinium (Gd) also absorbs X-ray radiation 2.5 times more than iodine, a widely used CT contrast agent in clinic,[31, 32] making it a promising candidate for CT imaging.[33, 34] Integrating of Au and Gd into a single scaffold, it is expected, may produce synergistic effects, leading to better CT imaging contrast than either Au or Gd alone.[35, 36] Meanwhile, Gd is a superior MRI nanotracer for cell tracking.[37] Thus, the combination of the two elements into a single nanoplatform may offer a potential strategy to realize CT/MR dual-modality imaging tracing of the stem cells after transplantation into the lung.

The cells are often reportedly labeled with CT and MRI contrast agents sequentially for CT/MR dual-modality imaging tracing of the transplanted stem cells *in vivo*.[27] However, this two-step labeling strategy is laborious and time-consuming.[38] To address these issues, we report herein synthesis of a CT/MR dual-modal nanotracer by formation of gold-gadolinium nanoclusters (Au/GdNC) through an albumin-mediated strategy, followed by overcoating of a silica shell (Au/GdNC@SiO_2), for labeling and tracking of human MSCs (hMSCs) after transplantation into PF murine model induced by bleomycin (**Figure 1**). Previous studies demonstrated that small-sized AuNCs have higher X-ray absorption performance and consequently exhibit better CT imaging contrast than the large-sized AuNPs.[30] The overcoating of a silica layer, it is expected, not only enhances the imaging contrast of the Au/GdNC@SiO_2 nanotracers,[39] but also improves its stability inside the labeled cells, and thus alleviates the dilution of nanotracer concentration in the cells caused by stem cell division. Altogether, thus-prepared Au/GdNC@SiO_2 nanotracer may exhibit enhanced CT and MR imaging contrast for efficient tracking of the labeled hMSCs in PF.

2. EXPERIMENTAL SECTION

2.1. Preparation of Au/GdNC@SiO_2. Au/GdNC stabilized by bovine serum albumin (BSA) was first obtained by a facile route.[40] Briefly, 5 mL of $HAuCl_4$ aqueous solution (10 mM) and 0.15 mL of $GdCl_3$ aqueous solution (500 mM) were added to 5 mL of BSA solution (50 mg mL^{-1}) under vigorous stirring, the mixture was stirred at 37 ^{o}C for 10 min. Then, 0.75 mL of NaOH solution (1 M) was added, and the mixture was continuously stirred at 37 ^{o}C for 12 h.

The Au/GdNC@SiO_2 nanotracer was obtained via modified Stöber method.[40] Typically, 300 μL of Au/GdNC (3 mM of Au) aqueous solution was added into 20 mL of ethanol solution (containing 800 μL of $NH_3{\cdot}H_2O$) under stirring. After 5 min, 200 μL of tetraethylorthosilicate (TEOS) was added under stirring. After 1 h, another 200 μL of TEOS was introduced under stirring. Then, the mixture solution was stirred at room temperature for 24 h. Au/GdNC@SiO_2 nanotracer was collected by centrifugation at 9,000 rpm and then washed with ethanol and deionized water for several times until the pH = 7. The purified Au/GdNC@SiO_2 nanotracer was redispersed into deionized water for further experiments.

2.2. Characterization of Au/GdNC@SiO_2. The morphology and size of

Au/GdNC@SiO_2 were characterized using transmission electron microscopy (TEM, Tecnai G2 F20 S-Twin TEM) at an accelerating voltage of 200 kV, and a particle size analyzer (ZEN3600-nanoZS, Malvern), respectively. An inductively coupled plasma mass spectrometer (ICP-MS, Thermo Fisher Scientific) was used for the quantitative analysis of element concentration. X-ray photoelectron spectroscopy (XPS) data were obtained from a Thermo Esca lab 250 XPS equipment using monochromatic Al Kα radiation (hn = 1486.6 eV). All binding energies were referenced to the extraneous carbon C1s peak (284.6 eV). CT imaging was performed by a Micro-CT imager (Hiscan XM). The parameters for scanning were according to our previous study.[16] *In vitro* MRI measurement was obtained using NMR analyzer (GY-PNMR-10, 0.5 T). T_1 relaxation time of the solution samples was measured with the inversion recovery method (repetition time (TR) = 10 s). Longitudinal relaxivity (r_1) was calculated by the linear fitting of $1/T_1$ versus Gd (III) concentration. T_1-weighted MR imaging was obtained with spin-echo sequence under the following parameters: TR = 100.0 ms, echo time (TE) = 8.6 ms, and the number of scans (NS) = 1. The curve fitting of $1/T_1$ (s^{-1}) versus the gadolinium concentration was performed to get the value of longitudinal relaxivity (r_1).

2.3. Cell Culturing. MSCs derived from the human umbilical cord (hMSCs) were generously offered by Suzhou Jiulong Hospital (Suzhou, China). The hMSCs (passages 3-8) were cultivated with DMEM/F12 basic medium, which was supplemented with penicillin-streptomycin (1%) and fetal bovine serum (10%). The hMSCs were cultivated in a carbon dioxide incubator (Thermo 3111).

2.4. Labeling hMSCs with Au/GdNC@SiO_2. The hMSCs (1×10^6 cells per dish) were cultured in plastic cell culture dishes with 100 mm × 20 mm style (Corning Co. LTD.) for 24 h. For electroporation (EP) labeling, the hMSCs precipitate was obtained by trypsinizing and centrifuging at 800 rpm for 4 min. The cell precipitates were resuspended in EP-buffer (200 μL, Etta Biotech, China) containing Au/GdNC@SiO_2 at different Au concentrations (0.075, 0.15, 0.3, 0.6, 0.9 and 1.2 mM), and then transferred to 96-well plate. Then the cells were EP-labeled using the X-Porator® EBXP-H1 (Etta Biotech, China). The labeling parameters were set as follows: voltage = 110 V, pulses = 100 μs, time interval = 1 s, and the number of EP-labeling = 6. Afterward, the cells were transferred in 2 mL of DMEM/F12 basic medium and recovered for 15 min. After that, the hMSCs were washed with culture medium for three times to remove the residual material at 800 rpm for 4 min. Then the precipitated cells were suspended in DMEM/F12 medium for future use.

2.5. Measurement of the Intracellular Au and Gd Contents. Cellular Au and Gd contents were detected by ICP-MS. The hMSCs labeled with Au/GdNC@SiO_2 were digested with 1 mL of *aqua regia* (mixture of HNO_3 and HCl at the volume ratio of 1:3). Then the samples were diluted with deionized water to 10 mL. ICP-MS was applied to analyze the concentrations of Au and Gd. All the tests were repeated three times in parallel and the average value was recorded.

2.6. TEM of the Labeled Cells. TEM was used to evaluate the intracellular distribution of Au/GdNC@SiO_2 after EP labeling. The labeled hMSCs were stained with 1% OsO_4, dehydrated in an acetone gradient, immersed in acetone solution containing epoxy resin for 1 h, and cured at 60 ^oC for 24 h. The cells were then transferred into epoxy resin, fixing for 2 h. After that, the samples were put in a furnace at 70 ^oC for 2 d to polymerize the epoxy resin, and then were sliced using a microtome. Each slice was put on a grid for TEM characterization.

2.7. Cell Viability and Proliferation Analysis. The cell counting kit-8 (CCK-8) assay was implemented to evaluate the viability and proliferation of the hMSCs after labeling. This assay was detected in triplicate. For viability test, the hMSCs (5,000 cells per well) EP-labeled with Au/GdNC@SiO_2 at diverse Au contents (0.075, 0.15, 0.3, 0.6, 0.9, 1.2 and 1.5 mM) were first seeded into 96-well plates, incubating for 24 h. After that, the cell viability was tested by CCK-8. And the microplate reader was used to record the absorbance value at 450 nm. The hMSCs without labeling were used as control.

In the proliferation test, the hMSCs were first labeled with Au/GdNC@SiO_2 (1.2 mM of Au) by EP labeling. After labeling, the hMSCs were transferred into 24-well plates, and each well contained 1×10^4 cells. After maintaining for 24 h, the cell growth profile was monitored by CCK-8. The absorbance intensity at 450 nm was monitored for 7 d. The hMSCs without EP labeling were act as the control.

2.8. Osteogenic and Adipogenic Differentiation Assay. The differentiation capacity of Au/GdNC@SiO_2 labeled hMSCs was examined by histological analysis. The hMSCs were first EP-labeled with Au/GdNC@SiO_2 (1.2 mM of Au). After that, the labeled hMSCs were cultured into 24-well plates, and each well contained 1×10^4 cells. After culturing for 24 h, the hMSCs were washed twice with PBS. Then the hMSCs were further cultured for three weeks with osteogenic induction differentiation complete medium (Cyagen Biosciences Inc.), which was prepared on the basis of the directions of manufacturer, to induce osteogenic differentiation. Afterward, the cells were treated with paraformaldehyde (4%) and stained by Alizarin Red S (an organic dye that can react with calcium nodules in osteoblasts to produce a dark red colored compound). After staining, the samples were washed with PBS. The laser confocal microscope was performed to observe calcium nodules. For quantitative detection, the dye in the stem cells was dissolved using dimethyl sulfoxide (DMSO), and then the absorbance value at 550 nm was recorded by a microplate reader. The hMSCs without any labeling were taken as control.

To produce adipogenic differentiation, the labeled hMSCs were cultivated with adipogenic differentiation induction medium and adipogenic differentiation maintenance medium (Cyagen Biosciences Inc), which were prepared in accordance with the directions of manufacturer, for 3 d and 1 d, respectively. After repeating the procedure for 4-5 times, the cells were cultured using maintenance medium for 5-7 d, and then treated with paraformaldehyde (4%) and stained with Oil Red O (a dye for fat staining) for 30 min, washing with PBS for three times. The laser confocal microscope was applied to observe the formation of lipid droplets. For quantitative detection, the dye in cells was dissolved in DMSO, and the absorbance intensity at 490 nm was measured by a microplate reader.

2.9. Animal Model. The animal experiment was approved by the Animal Ethics Committee of Suzhou Institute of Nano-Tech and Nano-Bionics, Chinese Academy of

Sciences (Suzhou, China). C57BL/6 mice (male, 10 weeks old, about 30 g) purchased from Suzhou Industrial Park Elmet technology Co. Ltd. were administrated with bleomycin (BLM) as described.[41] Briefly, the mice were divided into two groups: the saline control group (n = 5) and the BLM group (n = 15). Those mice of the BLM group were administrated with 50 μL of BLM (2 mg kg^{-1} each mouse) intratracheally to induce PF, while the mice of the control group were given saline (50 μL) instead. After 7, 14 and 21 d, the gross lung morphologies of the control group and BLM group (n = 5 for each time point) were observed by hematoxylin-eosin (HE) and Masson's trichrome staining. For hMSCs tracking, the BLM-treated mice (n = 5) were transplanted with the Au/GdNCs@SiO_2 (2.4 mM of Au) labeled hMSCs (2×10^6 cells in 100 μL of saline each mouse) via intratracheal injection at the 7 d post-instillation of BLM. For hMSCs therapy, BLM-treated mice (n = 5 for each group) were transplanted with either unlabeled or labeled hMSCs (2×10^6 cells in 100 μL of saline for each mouse), respectively, via intratracheal injection at 7 d post-instillation of BLM. The mice treated with saline (the control group, n = 5) and the BLM-treated mice without hMSCs therapy (BLM group, n = 5) were used for comparison. After 7 d, the gross lung morphologies of the control group, the BLM group and the hMSCs therapy group (treated with unlabeled or labeled hMSCs) were observed by Masson's trichrome staining, respectively. Hydroxyproline (HYP) assay was used for analyzing the collagen content in lung tissues as previously described.[42]

2.10. *In Vitro* and *In Vivo* CT/MR Imaging. For *in vitro* imaging, the EP-labeled hMSCs (2×10^6 cells) were washed and centrifuged to form precipitated cells. Then the cells were transferred into capillary tubes (1.0 mm-i.d.), and centrifuged at 800 rpm for 4 min to produce 2 cm height for cells at the bottom of the capillary. According to this method, the cell density can reach 1.3×10^8 cells mL^{-1}, which is analogous to that in many tissues ($1.5\sim3 \times 10^8$ cells mL^{-1}).[43] The parameters of cellular CT and MR imaging were described as above.

Micro-CT scanning *in vivo* was carried out at 3 h, 1 d, 3 d, and 7 d, respectively, after tracheal injection of the labeled hMSCs into the BLM-treated mice at 7 d post-instillation of BLM. The micro-CT equipment was described as above. After CT scanning, the mice were processed *in vivo* MRI scanning immediately, placing in the 1.5 T imaging systems (35 °C). The detailed MR imaging experimental condition was set as follows: number excitation = 1; TR/TE = 100/16.8 ms; matrix = 512 × 256; slice thickness = 0.3 mm; 128 slices and no gap between slices.

2.11. Quantitative Analysis of CT Data. The Hounsfield unit (HU) value reflects the degree of X-ray absorption of the tissue, which is usually used for quantitative analysis of CT images.[44] The *in vitro* HU is obtained by linear extrapolation using

$$\mathrm{HU} = 1000 \times \frac{\mu_x - \mu_{water}}{\mu_{water} - \mu_{air}} \qquad (1)$$

where μ_x, μ_{water}, and μ_{air} are the attenuation coefficients of the sample, water, and air obtained from CT scanning, respectively.[16]

To evaluate the average CT values (HU) of the transplanted hMSCs in the lung, the CT signal intensity of myocardial was applied to adjust the attenuation value.[45] The *in vivo* HU value could be obtained by using the formula:

$$\mathrm{HU} = \frac{1040 \times (\mu_x - \mu_m)}{\mu_m - \mu_{air}} + 40 \qquad (2)$$

where μ_x, μ_m, and μ_{air} represent the attenuation coefficients of the regions of interest (ROI), myocardial, and air showed in CT equipment, respectively.

2.12. Statistical Analysis. The *in vitro* data are expressed as the mean ± standard deviation (SD) of three independent trials. Statistical comparisons between two groups were performed via Student's t-test. Multiple group comparisons were made using a one-way analysis of variance (ANOVA), in which $P < 0.05$ was considered statistically significant.

3. RESULTS AND DISCUSSION

3.1. Synthesis and Characterization of Au/GdNC@SiO_2 Nanotracer. The principle of the synthesis of Au/GdNC@SiO_2 is shown in **Figure 1**. Firstly, the Au/GdNC was synthesized using BSA as the scaffold via the ambient biomineralization approach as reported by Le et al..[40] Briefly, BSA was added to the mixed solution of $HAuCl_4$ and $GdCl_3$ under vigorous stirring. BSA contains lots of active groups such as sulfhydryl and carboxyl groups, which have a strong affinity to metal ions.[46] After adding NaOH, the BSA extended at pH 12 through the unfolding process, triggering the reduction capability of the amino acid. To ensure the complete reduction of $HAuCl_4$ and $GdCl_3$ by BSA, the reaction mixture was stirred for 12 h at 37 °C, obtaining Au/GdNC. The size and morphology of thus-obtained Au/GdNC were characterized by TEM. The results showed that the spherical hybrid NC had a size of 4.9 nm ± 1.1 nm with good monodispersity (**Figure 2**B), much bigger than AuNC (less than 2.0 nm, **Figures 2**A and **S1**A), which was attributed to the involvement of Gd in the formation of the hybrid NC. However, the hydrodynamic size of Au/GdNC was 14.7 nm with narrow size distribution (**Figure S1**B), which was much larger than that observed from the TEM imaging, due to the hydration of the particles.[47]

Secondly, Au/GdNC@SiO_2 nanotracer was prepared by overcoating of a silica shell onto the surface of Au/GdNC following the modified Stöber method.[39] From the TEM imaging, the size of Au/GdNC@SiO_2 was determined to be about 35.9 nm ± 2.4 nm (**Figure 2**C), and the hydrodynamic diameter of Au/GdNC@SiO_2 increased to 90.6 nm (**Figure 2**D), due to the overcoating of the silica shell. It was noticed that the hydrodynamic diameter showed little change within 7 d (**Figure S2**), implying good colloidal stability of Au/GdNC@SiO_2, which was beneficial to their biomedical applications. Furthermore, the surface potential of Au/GdNC@SiO_2 was determined to be -28.1 mV, which was more negative than that of Au/GdNC (-19.1 mV). In our work, the hMSCs were labeled with the nanotracer via electroporation-labeling technique, which was not affected significantly by the surface potential of the nanotracer.

The XPS results displayed the oxidation states of the Au and Gd elements in AuNC and Au/GdNC, respectively. As shown in **Figure S3**A and **S3**B, the $4f_{7/2}$ and $4f_{5/2}$ peaks of Au in Au/GdNC could be observed at binding energies of 83.8 eV and 87.5 eV, respectively, which were similar to that of Au in AuNC.[40] In addition, the XPS peaks of Gd in Au/GdNC appeared at 143.3 eV and 167.3 eV, respectively, attributing to the 4d region of Gd (**Figure S3**C). However, no characteristic peak for the 4d region of Gd was observed in XPS of AuNC (**Figure S3**D). These results indicated the successful formation of Au/GdNC.

Both Au and Gd elements have high X-ray attenuation due to their high atom number and electron density, and therefore are ideal CT contrast agents.[32] Moreover, the signal of CT imaging is proportional to the element content.[7] In order to obtain optimal CT imaging contrast of Au/GdNC, the feeding ratio of $HAuCl_4$ to $GdCl_3$ was adjusted in the synthesis of Au/GdNC. The molar ratio of Au to Gd (1:0.75, 1:1.4, 1:2, 1:3) in Au/GdNC decreased with the decrease in the feeding ratio of $HAuCl_4$ to $GdCl_3$ (1:0.5, 1:1, 1:1.5, 1:2), as evidenced by the ICP-MS measurement (**Table S1**). Nonetheless, the lower feeding ratio of $HAuCl_4$ to $GdCl_3$ (1:2.5) did not alter the molar ratio of Au to Gd (1:3) in Au/GdNC any more, suggesting the maximum loading of Au and Gd on BSA. Then, the X-ray attenuation coefficient was estimated for Au/GdNC with different feeding ratio of $HAuCl_4$ to $GdCl_3$. As indicated in **Figure S4**, the X-ray attenuation coefficients of Au/GdNC were measured to be 24.36, 39.05, 40.80, 32.36 and 32.75, respectively, for the feeding ratio of $HAuCl_4$ to $GdCl_3$ at 1:0.5, 1:1, 1:1.5, 1:2, 1:2.5. Au/GdNC exhibited the highest X-ray attenuation coefficient when the feeding ratio of $HAuCl_4$ to $GdCl_3$ was 1:1.5 (molar ratio of Au to Gd was 1:2 in Au/GdNC). With the Gd concentration increasing, the X-ray attenuation coefficient of Au/GdNC reduced. This could be explained by that the Gd gradually occupied the reaction site of Au on BSA with the increase in $GdCl_3$ concentration. However, the K-edge energy of Gd (50.2 keV) was significantly lower than that of Au (80.7 keV), resulting in the decreased X-ray attenuation coefficient of Au/GdNC.[48] Therefore, in the following experiment, the feeding ratio of $HAuCl_4$ to $GdCl_3$ was set to 1:1.5 in the preparation of Au/GdNC.

In addition, compared to AuNC, Au/GdNC exhibited significantly enhanced X-ray attenuation coefficient (**Figure 3**A and **3**B), implying that the existence of Gd in the hybrid nanotracer contributed to the enhancement of X-ray attenuation, although the K-edge energy of Gd was much lower than that of Au.[48] After the coating of the silica shell, the X-ray attenuation coefficient of Au/GdNC@SiO_2 further increased, being 5.6 times and 42 times as much as that of Au/GdNC and Ioversol (CT imaging contrast medium commonly used in clinic), respectively (**Figure 3**C and **3**D), mainly due to the aggregation of Au/GdNCs in Au/GdNCs@SiO_2.[39, 49] Moreover, with the increase of Au concentration, all the three types of nanotracers, AuNC, Au/GdNC, and Au/GdNC@SiO_2 displayed brighter CT images. These findings indicated that the combination of two radiodense elements within one system improved the X-ray attenuation property via synergetic effect, and that the overcoating of a silica layer onto Au/GdNC surface could further enhance the CT imaging contrast of the nanotracer. Moreover, to assess the chemical stability, the Au/GdNC@SiO_2 nantracers were dialyzed against distilled water over 7 days, and the distilled water was changed every 24 h. As presented in **Table S2**, there was only a slight change in the concentrations of Au and Gd in Au/GdNC@SiO_2 for 7-day dialysis, suggesting good chemical stability of the nanotracer.

To evaluate whether the Au/GdNC@SiO_2 could act as a valid MRI nanotracer, the longitudinal (T_1) relaxation time was measured with a 0.5 T NMR analyzer at different Gd concentrations. As presented in **Figure 3**E, the Au/GdNC showed a high r_1 value of

8.68 s^{-1} per mM of Gd in PBS, from the linear fitting of the plot of $1/T_1$ *vs* Gd concentration, which was nearly twice as large as that of Magnevist (3.80 mM^{-1} s^{-1}), one of the most widely used MRI contrast agent in clinic.[37] Interestingly, Au/GdNC@SiO_2 exhibited a substantially higher value of r_1 (24.62 mM^{-1} s^{-1}) than Au/GdNC (8.68 mM^{-1} s^{-1}) (**Figure 3**F). The dramatically increased relaxivity might be due to the formation of Au/GdNC aggregates encapsulated by the silica shell. T_1-weighted MR images and the corresponding signal intensity further demonstrated the enhanced T_1 imaging signal of Au/GdNC@SiO_2 (Inset images in **Figure 3**F). Therefore, the silica coating not only improved the chemical stability of the nanotracer, but also enhanced the imaging contrast of the composite nanoparticles. The above results demonstrated clearly that Au/GdNC@SiO_2 could act as a high-efficiency CT/MR nanotracer.

3.2. Au/GdNC@SiO_2 Labeling and Its Effects on the Viability, Proliferation, and Differentiation of the hMSCs. EP-labeling is widely used in cellular biology to deliver hydrophilic xenobiotics into cells.[50] Furthermore, EP-labeling has been demonstrated to be a sustainable and cell biology preserving labeling method for MSCs.[51] To evaluate whether the hMSCs could be labeled with Au/GdNC@SiO_2 via the EP-labeling technique, the cellular TEM imaging was performed. **Figure 4**A displays the TEM images of hMSCs after EP-labeling with Au/GdNC@SiO_2 at once. After EP-labeling, Au/GdNC@SiO_2 entered into the labeled hMSCs and mainly gathered on the cell membrane, which appeared to be fragmented. After 1 d culture and recovery of the labeled hMSCs, the Au/GdNC@SiO_2 nanotracers continued to migrate into the cell inner, and were mainly distributed in the cytoplasm. The cell membrane recovered to its regular shape (**Figure 4**B), which was consistent with the observation in literature.[52]

To evaluate whether the cell viability and proliferation might be affected by Au/GdNC@SiO_2 labeling, the EP-labeled and unlabeled hMSCs were analyzed. As shown in **Figure 5**A, the Au/GdNC@SiO_2 labeled hMSCs showed inconspicuous cytotoxicity with the Au content range from 0 to 1.2 mM. However, further increasing of the Au concentration (1.5 mM) led to obvious cytotoxicity. Therefore, in the experiments below, Au/GdNC@SiO_2 at the Au concentration of 1.2 mM was adopted for EP-labeling of hMSCs. As shown in **Figure 5**B, there was no visible dissimilarity in proliferation behavior between the EP-labeled and the unlabeled hMSCs, indicating that Au/GdNC@SiO_2 EP-labeling imposed no significant influence on the proliferation of the hMSCs.

Next, to assess whether or not the Au/GdNC@SiO_2 labeling influences with the cell differentiation potential, the EP-labeled hMSCs were induced to differentiate into osteoblasts and adipocytes, respectively. The hMSCs labeled with Au/GdNC@SiO_2, our experiment demonstrated, displayed osteogenic differentiation behavior analogous to the unlabeled hMSCs. Both the unlabeled and the EP-labeled hMSCs produced calcium nodules, the dark red deposits in **Figure 5**C, after Alizarin Red S staining. Similar osteogenic differentiation behavior was further supported by quantitative analysis (**Figure 5**D). Moreover, the absorbance intensity of Oil Red O extracted from the unlabeled and the EP-labeled hMSCs lysates at 490 nm exhibited invisible difference, indicating the similar adipogenesis between the unlabeled and the EP-labeled hMSCs (**Figure 5**E and **5**F). In short, the multipotent performance of the hMSCs was not affected by Au/GdNC@SiO_2 labeling, indicating the prominent biological safety of Au/GdNC@SiO_2.

3.3. *In Vitro* CT/MR Imaging of Labeled hMSCs. To evaluate the CT/MR imaging performance of the hMSCs after labeling, the hMSCs were EP-labeled with Au/GdNC@SiO_2 at diverse Au contents, then washed and harvested into 1.0 mm-i.d. capillary tubes, reaching a cell density (1.3×10^8 cells mL^{-1}) close to that of tissue ($1.5\sim3 \times 10^8$ cells mL^{-1}).[43] As the micro-CT imaging displayed, the labeled hMSCs displayed stronger attenuation than the unlabeled hMSCs (78 HU) (**Figure 6**A). The CT values were measured to be 88, 154, 273, 380, and 648 HU, respectively, for the hMSCs EP-labeled with Au/GdNC@SiO_2 at the intracellular Au concentration of 7.22, 14.30, 34.80, 43.77 and 97.50 μg mL^{-1}, suggesting that the CT signal was depended on the intracellular Au content of the labeled hMSCs (**Figure 6**A). Moreover, the labeled hMSCs displayed significantly enhanced MRI contrast compared to the unlabeled hMSCs (**Figure 6**B). As the Gd concentration increased, the T_1 MRI phantoms gradually brightened, showing a dose-dependent behavior. Taken together, the Au/GdNC@SiO_2 labeled hMSCs showed good *in vitro* CT/MR dual-modal imaging performance.

3.4. Establishment of BLM-Induced PF Murine Model. The PF murine model was used for hMSCs tracking in C57BL/6 mice which were intratracheal injected with BLM (2 mg kg^{-1}). HE and Masson's trichrome stainings were applied to estimate the gross lung morphologies (**Figure S5**). In the next 7, 14 and 21 d after BLM instillation, the BLM-treated mouse revealed severe tissue injury with massive immune cell infiltration, and loss of normal alveolar, bronchi, and vasculature, as evidenced by the HE staining results shown in **Figure S5**. In addition, an increasing aggregation of collagen fiber deposition was observed in the lung of the BLM-treated mouse in the next 7, 14 and 21 d post-treatment, in comparison with that in the lung of the saline-treated mouse group (Masson's trichrome staining in **Figure S5**). The pathological changes showed from HE and Masson's trichrome stainings with time increasing indicated the successful pulmonary fibrosis modeling. In this work, *in vivo* cell tracking experiment was performed at 7 d post-injection of BLM, because hMSCs treatment was suitable for the early stage of PF.[53]

3.5. *In Vivo* CT/MR Imaging of Labeled hMSCs. To validate the feasibility of CT/MR imaging tracking of the transplanted hMSCs *in vivo*, the Au/GdNC@SiO_2 labeled hMSCs (2×10^6 cells) suspended in saline (100 μL) were injected into the lung of PF murine model *via* intratracheal injection. After the injection, the mouse was examined immediately by micro-CT and subsequent MRI scanning. **Figure 7**A reveals the CT and MR images at 3 h, 1 d, 3 d, and 7 d post-transplantation of the labeled hMSCs, while the CT and MR images obtained before transplantation were taken as control. After the transplantation of the labeled hMSCs, the lung tissue exhibited significant CT imaging signals at 3 h post-transplantation. The *in vivo* average CT values of the transplanted hMSCs were calculated from three ROI. The CT values were measured to be -138 (before transplantation), 80 (after transplantation at 3 h), 217 (after transplantation at 1 d), 66 (after transplantation at 3 d), and -97 (after transplantation at 7 d) HU, respectively (**Figure S6**). After injection of the labeled hMSCs, the CT values increased with time, and reached maximum at 1 d, and then decreased gradually in the next 7 d. However, significant MRI signals were obtained from the whole lung at 3 h post-transplantation of the labeled hMSCs compared to the control. The labeled hMSCs could be observed from all of the lung as MRI results showed. Since the detection sensitivity of MRI is much higher than that of CT imaging,[54] the effective dose of the MRI component (in the micromolar level) is much lower than that of the corresponding CT component (in the millimolar level) in the nanotracers.[7] Thus, at the same concentration of the nanotracers, MRI signals were much easier to be observed than CT signals. However, the spatial resolution of MRI signals was much lower than that of CT signals. Similarly, the intensity of MRI signals gradually decreased in the next 3 d and 7 d after injection of the labeled hMSCs. The labeled hMSCs kept division after transplantation, which led to the dilution of nanotracer, and as a consequence, decreased the detection sensitivity and the signal intensity.[7] To confirm whether or not the Au/GdNC@SiO_2 still stayed in the labeled hMSCs after transplantation, the PF mouse was sacrificed at 7 d post-transplantation, and the lung tissue was extracted to prepare frozen sections after dehydration. The Au/GdNC@SiO_2 was pre-tagged with rhodamine B isothiocyanate (RBITC), a fluorescent dye. And the cell membrane dye 3,3'-dioctadecyloxacarbocyanine perchlorate (DiO) was used to mark hMSCs before transplantation. The fluorescence confocal microscopy images display that the red fluorescence region (RBITC-Au/GdNC@SiO_2) matched well with the green fluorescence region (DiO), distinctly demonstrating the presence of Au/GdNC@SiO_2 in the labeled hMSCs. Consequently, it is clear that the imaging signals were true signal of the labeled cells (**Figure 7**B). In brief, the above results demonstrated that the hMSCs labeling with Au/GdNC@SiO_2 could be tracked for 7 d v*ia* CT/MR imaging after transplantation in the lung.

3.6. Effect of hMSCs on the Therapeutic Efficacy of BLM-Induced Pulmonary Fibrosis. PF is a severe lung disease with high mortality. However, there remains a lack of effective therapies for PF. The hMSCs have been proven promising in tissue engineering by migrating to the damaged tissue to facilitate tissue repair.[3-5] To evaluate whether or not the labeled hMSCs mitigate the symptoms of pulmonary fibrosis, hMSCs (2×10^6 cells) were transplanted into the lung of the BLM-treated mice *via* intratracheal instillation at 7 d post-injection of BLM, and the histological analysis was performed at 7 d post-transplanted of the labeled hMSCs. Masson's trichrome staining of the lung sections indicated that the collagen fiber deposition decreased after the transplantation of the unlabeled or the labeled hMSCs, which was confirmed by HYP assay (**Figures 8** and **S7**). However, the BLM group without hMSCs transplantation did not show any improvement. Thus, the administration of hMSCs, no matter whether the labeled or the unlabeled hMSCs, relieved and ameliorated BLM-induced histopathological damage.

4. CONCLUSIONS

A CT/MR dual-modal nanotracer, Au/GdNC@SiO_2, was developed and used to label and track the hMSCs in the lung. The integration of Au and Gd elements into the nanotracer led to substantially improved CT and MR signals, with 42 times increase in X-ray attenuation coefficient and 6.5 times increase in MR r_1 relaxivity, respectively, compared to clinically used Ioversol and Magnevist. Particularly, the Au/GdNC@SiO_2 nanotracer exhibited high labeling efficiency for hMSCs via electroporation without affecting their viability, proliferation, and differentiation capacity. With a PF murine model, the transplanted hMSCs were tracked for 7 d *in vivo via* CT/MR dual-modal imaging by Au/GdNC@SiO_2 nanotracer labeling. Furthermore, a preliminary experiment with the lung sectioning results showed that the labeled hMSCs significantly alleviated the PF after being transplanted to the BLM treated mice. This work highlighted the promise of Au/GdNC@SiO_2 as an efficient and safe CT/MR dual-modal nanotracer for *in vivo* hMSC tracking, and consequently, may provide a powerful and convenient tool to monitor the transplanted hMSCs *in vivo*, and further guide the stem cell-based therapy in tissue engineering and regenerative medicine.

ASSOCIATED CONTENT

Supporting Information

The molar concentrations of Au and Gd in Au/GdNC; The concentrations of Au and Gd in aqueous solution of Au/GdNC@SiO_2 dialyzed for different time points; Dynamic light scattering data of AuNC and Au/GdNC; Dynamic light scattering data of Au/GdNC@SiO_2; X-ray photoelectron spectroscopy spectra of nanotracer; Plot of calculated HU values of Au/GdNC with different feeding ratio of $HAuCl_4$ to $GdCl_3$ as a function of the Au concentration; BLM-treated lung sections after administration of BLM; The CT values of the Au/GdNC@SiO_2 labeled hMSCs before and after transplantation; Hydroxyproline content in the lung of the BLM-induced PF mouse.

AUTHOR INFORMATION

Corresponding Authors

*E-mail: chaojie@seu.edu.cn

*E-mail: zjzhang2007@sinano.ac.cn

Notes

The authors declare no competing financial interest.

ACKNOWLEDGEMENTS

This work was supported by the National Natural Science Foundation of China (81801769), National Key R&D Program of China (2017YFA0104301, 2017YFA0104303), Jiangsu Provincial Fund for Natural Sciences (BK20180257), and Science and technology development plan project of Suzhou (SYG201851). We thank Professor Shouhua Luo, Southeast University, for assistance in CT data analysis.

REFERENCES:

(1) Li, G. Q.; Jin, F. Q.; Du, J. X.; He, Q. J.; Yang, B.; Luo, P. H. Macrophage-Secreted TSLP and MMP9 Promote Bleomycin-Induced Pulmonary Fibrosis. *Toxicol. Appl. Pharmacol.* **2019**, *366*, 10-6.

(2) Ortiz, L. A.; Gambelli, F.; McBride, C.; Gaupp, D.; Baddoo, M.; Kaminski, N.; Phinney, D. G. Mesenchymal Stem Cell Engraftment in Lung is Enhanced in Response to Bleomycin Exposure and Ameliorates Its Fibrotic Effects. *Proc. Natl. Acad. Sci.* **2003**, *100*, 8407-8411.

(3) Zhang, W. G.; He, L.; Shi, X. M.; Wu, S. S.; Zhang, B.; Mei, L.; Xu, Y. J.; Zhang, Z. X.; Zhao, J. P.; Zhang, H. L. Regulation of Transplanted Mesenchymal Stem Cells by the Lung Progenitor Niche in Rats with Chronic Obstructive Pulmonary Disease. *Respir. Res.* **2015**, *15*, 33.

(4) Wang, C.; Zhu, H. M.; Sun, Z. R.; Xiang, Z.; Ge, Y. Y.; Ni, C.; Luo, Z. W.; Qian, W. P.; Han, X. D. Inhibition of Wnt/β-Catenin Signaling Promotes Epithelial Differentiation of Mesenchymal Stem Cells and Repairs Bleomycin-Induced Lung Injury. *Am. J. Physiol. Cell Physiol.* **2014**, *307*, C234-C244.

(5) Jiang, Y. H.; Jahagirdar, B. N.; Reinhardt, R. L.; Schwartz, R. E.; Keene, C. D.; Ortiz-Gonzalez, X. R.; Reyes, M.; Lenvik, T.; Lund, T.; Blackstad, M.; Du, J. B.; Aldrich, S.; Lisberg, A.; Low, W. C.; Largaespada, D. A.; Verfaillie, C. M. Pluripotency of Mesenchymal Stem Cells Derived from Adult Marrow. *Nature* **2002**, *418*, 41-49.

(6) Hess, D. C.; Borlongan, C. V. Cell-Based Therapy in Ischemic Stroke. *Expert Rev.*

Neurother. **2008**, *8*, 1193-1201.

(7) Meri, R.; Popovtzer, R. Cell Tracking Using Gold Nanoparticles and Computed Tomography Imaging. *Wiley Interdiscip. Rev. Nanomed. Nanobiotechnol.* **2018**, *10*, e1480.

(8) Kircher, M. F.; Gambhir, S. S.; Grimm, J. Noninvasive Cell-Tracking Methods. *Nat. Rev. Clin. Oncol.* **2011**, *8*, 677-688.

(9) Chin, B. B.; Nakamoto, Y.; Bulte, J. W. M.; Pittenger, M. F.; Wahl, R.; Kraitchman, D. L. 111In Oxine Labelled Mesenchymal Stem Cell SPECT after Intravenous Administration in Myocardial Infarction. *Nucl. Med. Commun.* **2003**, *24*, 1149-1154.

(10) Ahrens, E. T.; Bulte, J. W. M. Tracking Immune Cells in Vivo Using Magnetic Resonance Imaging. *Nat. Rev. Immunol.* **2013**, *13*, 755-763.

(11) Bulte, J. W. M.; Walczak, P.; Janowski, M.; Krishnan, K. M.; Arami, H.; Halkola, A.; Gleich, B.; Rahmer, J. Quantitative "Hot Spot" Imaging of Transplanted Stem Cells Using Superparamagnetic Tracers and Magnetic Particle Imaging. *Tomography* **2015**, *1*, 91-97.

(12) Zheng, B.; Vazin, T.; Goodwill, P. W.; Conway, A.; Verma, A.; Saritas, E. U.; Schaffer, D.; Conolly, S. M. Magnetic Particle Imaging Tracks the Long-Term Fate of in Vivo Neural Cell Implants with High Image Contrast. *Sci. Rep.* **2015**, *5*, 14055.

(13) Kim, T.; Lee, N.; Arifin, D. R.; Shats, I.; Janowski, M.; Walczak, P.; Hyeon, T.; Bulte, J. W. M. In Vivo Micro-CT Imaging of Human Mesenchymal Stem Cells Labeled with Gold-Poly-L-Lysine Nanocomplexes. *Adv. Funct. Mater.* **2017**, *27*, 1604213.

(14) Ito, T.; Itakura, S.; Todorov, I.; Rawson, J.; Asari, S.; Shintaku, J.; Nair, I.; Ferreri, K.; Kandeel, F.; Mullen, Y. Mesenchymal Stem Cell and Islet Co-Transplantation Promotes Graft Revascularization and Function. *Transplantation* **2010**, *89*, 1438-1445.

(15) Wu, T. J.; Tzeng, Y. K.; Chang, W. W.; Cheng, C. A.; Kuo, Y.; Chien, C. H.; Chang, H. C.; Yu, J. Tracking the Engraftment and Regenerative Capabilities of Transplanted Lung Stem Cells Using Fluorescent Nanodiamonds. *Nat. Nanotechnol.* **2013**, *8*, 682-689.

(16) Bao, H. Y.; Xia, Y. Y.; Yu, C. G.; Ning, X. Y.; Liu, X. Y.; Fu, H.; Chen, Z. J.; Huang, J.; Zhang, Z. J. CT/Bioluminescence Dual-Modal Imaging Tracking of Mesenchymal Stem Cells in Pulmonary Fibrosis. *Small* **2019**, *15*, 1904314.

(17) Chen, G. C.; Liu, S. Y.; Huang, D. H.; Zhang, Y. J.; Li, C. Y.; Wang, M.; Wang, Q. B. Revealing the Fate of Transplanted Stem Cells In Vivo with a Novel Optical Imaging Strategy. *Small* **2018**, *14*, 1702679.

(18) Sharkey, J.; Scarfe, L.; Santeramo, I.; Garcia-Finana, M.; Park, B. K.; Poptani, H.; Wilm, B.; Taylor, A.; Murray, P. Imaging Technologies for Monitoring the Safety, Efficacy and Mechanisms of Action of Cell-Based Regenerative Medicine Therapies in Models of Kidney Disease. *Eur. J. Pharmacol.* **2016**, *790*, 74-82.

(19) Bhaskar, S.; Tian, F.; Stoeger, T.; Kreyling, W.; de la Fuente, J. M.; Grazú, V.; Borm, P.; Estrada, G.; Ntziachristos, V.; Razansky, D. Multifunctional Nanocarriers for Diagnostics, Drug Delivery and Targeted Treatment across Blood-Brain Barrier: Perspectives on Tracking and Neuroimaging. *Part. Fibre Toxicol.* **2013**, *7*, 3.

(20) Jakhmola, A.; Anton, N.; Anton, H.; Messaddeq, N.; Hallouard, F.; Klymchenko,

A.; Mely, Y.; Vandamme, T. F. Poly-ε-Caprolactone Tungsten Oxide Nanoparticles as a Contrast Agent for X-Ray Computed Tomography. *Biomaterials* **2014**, *35*, 2981-2986.

(21) Cao, J. S.; Wei, Y. H.; Zhang, Y. X.; Wang, G. L.; Ji, X.; Zhong, Z. Y. Iodine-Rich Polymersomes Enable Versatile SPECT/CT Imaging and Potent Radioisotope Therapy for Tumor in Vivo. *ACS Appl. Mater. Interfaces* **2019**, *11*, 18953-18959.

(22) Rabin, O.; Perez, J. M.; Grimm, J.; Wojtkiewicz, G.; Weissleder, R. An X-Ray Computed Tomography Imaging Agent Based on Long-Circulating Bismuth Sulphide Nanoparticles. *Nat. Mater.* **2006**, *5*, 118-122.

(23) Liu, Y.; He, Z. J.; Xu, B.; Wu, Q. Z.; Liu, G.; Zhu, H. Y.; Zhong, Q.; Deng, D. Y.; Ai, H.; Yue, Q.; Wei, Y.; Jun, S.; Zhou, G. Q.; Gong, Q. Y. Evaluation of Cell Tracking Effects for Transplanted Mesenchymal Stem Cells with jetPEI/Gd-DTPA Complexes in Animal Models of Hemorrhagic Spinal Cord Injury. *Brain Res.* **2011**, *1391*, 24-35.

(24) Agudelo, C. A.; Tachibana, Y.; Hurtado, A. F.; Ose, T.; Iida, H.; Yamaoka, T. The Use of Magnetic Resonance Cell Tracking to Monitor Endothelial Progenitor Cells in a Rat Hindlimb Ischemic Model. *Biomaterials* **2012**, *33*, 2439-2448.

(25) McQuade, C.; Al Zaki, A.; Desai, Y.; Vido, M.; Sakhuja, T.; Cheng, Z. L.; Hickey, R. J.; Joh, D.; Park, S. J.; Kao, G.; Dorsey, J. F.; Tsourkas, A. A Multifunctional Nanoplatform for Imaging, Radiotherapy, and the Prediction of Therapeutic Response. *Small* **2015**, *11*, 834-843.

(26) Lv, R. C.; Yang, P. P.; He, F.; Gai, S. L.; Li, C. X.; Dai, Y. L.; Yang, G. X.; Lin, J. A Yolk-Like Multifunctional Platform for Multimodal Imaging and Synergistic Therapy Triggered by a Single Near-Infrared Light. *ACS Nano* **2015**, *9*, 1630-1647.

(27) Kim, J.; Chhour, P.; Hsu, J.; Litt, H. I.; Ferrari, V. A.; Popovtzer, R.; Cormode, D. P. Use of Nanoparticle Contrast Agents for Cell Tracking with Computed Tomography. *Bioconjugate Chem.* **2017**, *28*, 1581-1597.

(28) Betzer, O.; Shwartz, A.; Motiei, M.; Kazimirsky, G.; Gispan, I.; Damti, E.; Brodie, C.; Yadid, G.; Popovtzer, R. Nanoparticle-Based CT Imaging Technique for Longitudinal and Quantitative Stem Cell Tracking within the Brain: Application in Neuropsychiatric Disorders. *ACS Nano* **2014**, *8*, 9274-9285.

(29) Jackson, P. A.; Abd Rahman, W. N. W.; Wong, C. J.; Ackerly, T.; Geso, M. Potential Dependent Superiority of Gold Nanoparticles in Comparison to Iodinated Contrast Agents. *Eur. J. Radiol.* **2010**, *75*, 104-109.

(30) Xu, C. J.; Tung, G. A.; Sun, S. H. Size and Concentration Effect of Gold Nanoparticles on X-Ray Attenuation as Measured on Computed Tomography. *Chem. Mater.* **2008**, *20*, 4167-4169.

(31) Lee, E. J.; Heo, W. C.; Park, J. W.; Chang, Y.; Bae, J. E.; Chae, K. S.; Kim, T. J.; Park, J. A.; Lee, G. H. D-Glucuronic Acid Coated $Gd(IO_3)_3 \cdot 2H_2O$ Nanomaterial as a Potential T_1 MRI-CT Dual Contrast Agent. *Eur. J. Inorg. Chem.* **2013**, *16*, 2858-2866.

(32) FitzGerald, P. F.; Colborn, R. E.; Edic, P. M.; Lambert, J. W.; Torres, A. S.; Bonitatibus, P. J.; Yeh, B. M. CT Image Contrast of High-Z Elements: Phantom Imaging Studies and Clinical Implications. *Radiology* **2016**, *278*, 723-733.

(33) Gierada, D. S.; Bae, K. T. Gadolinium as a CT Contrast Agent: Assessment in a Porcine Model. *Radiology* **1999**, *210*, 829-834.

(34) Badea, C. T.; Clark, D. P.; Holbrook, M.; Srivastava, M.; Mowery, Y.; Ghaghaha,

K. B. Functional Imaging of Tumor Vasculature Using Iodine and Gadolinium-Based Nanoparticle Contrast Agents: a Comparison of Spectral Micro-CT Using Energy Integrating and Photon Counting Detectors. *Phys. Med. Biol.* **2019**, *64*, 065007.

(35) Zhao, W. J.; Wang, Z. M.; Chen, L. N.; Huang, C. S.; Huang, Y. K.; Jia, N. Q. A Biomimetic Au@BSA-DTA Nanocomposites-Based Contrast Agent for Computed Tomography Imaging. *Mater. Sci. Eng. C* **2017**, *78*, 565-570.

(36) Liu, X. H.; Gao, C. H.; Gu, J. H.; Jiang, Y. F.; Yang, X. L.; Li, S. Y.; Gao, W.; An, T.; Duan, H. Q.; Fu, J. W.; Wang, Y. S.; Yang, X. Y. Hyaluronic Acid Stabilized Iodine-Containing Nanoparticles with Au Nanoshell Coating for X-Ray CT Imaging and Photothermal Therapy of Tumors. *ACS Appl. Mater. Interfaces* **2016**, *8*, 27622-27631.

(37) Fang, H.; Liu, C. Y.; Liu, C. Y.; Zhao, Z.; Safinya, C. R.; Qiao, W. H. Gd-DTPA-Dialkylamine Derivatives: Synthesis and Self-Assembled Behaviors for T_1-Enhanced Magnetic Resonance Imaging and Drug Carriers. *J. Mol. Liq.* **2018**, *268*, 77-86.

(38) Barnett, B. P.; Ruiz-Cabello, J.; Hota, P.; Ouwerkerk, R.; Shamblott, M. J.; Lauzon, C.; Walczak, P.; Gilson, W. D.; Chacko, V. P.; Kraitchamn, D. L.; Arepally, A.; Bulte, J. W. M. Use of Perfluorocarbon Nanoparticles for Non-Invasive Multimodal Cell Tracking of Human Pancreatic Islets. *Contrast Media Mol. Imaging* **2011**, *6*, 251-259.

(39) Huang, P.; Lin, J.; Wang, S. J.; Zhou, Z. J.; Li, Z. M.; Wang, Z.; Zhang, C. L.; Yue, X. Y.; Niu, G.; Yang, M.; Cui, D. X.; Chen, X. Y. Photosensitizer-Conjugated Silica-Coated Gold Nanoclusters for Fluorescence Imaging-Guided Photodynamic Therapy. *Biomaterials* **2013**, *34*, 4643-4654.

(40) Le, W. J.; Cui, S. B.; Chen, X.; Zhu, H. H.; Chen, B. D.; Cui, Z. Facile Synthesis of Gd-Functionalized Gold Nanoclusters as Potential MRI/CT Contrast Agents. *Nanomaterials* **2016**, *6*, 65.

(41) Ortiz, L. A.; Lasky, J.; Lungarella, G.; Cavarra, E.; Martorana, P.; Banks, W. A.; Peschon, J. J.; Schmidts, H. L.; Brody, A. R.; Friedman, M. Upregulation of the p75 But Not the p55 TNF-α Receptor mRNA After Silica and Bleomycin Exposure and Protection from Lung Injury in Double Receptor Knockout Mice. *Am. J. Respir. Cell Mol. Biol.* **1999**, *20*, 825-833.

(42) Bergman, I.; Loxley, R. Two Improved and Simplified Methods for the Spectrophotometric Determination of Hydroxyproline. *Anal. Chem.* **1963**, *35*, 1961-1965.

(43) Di Gregorio, E.; Ferrauto, G.; Gianolio, E.; Aime, S. Gd Loading by Hypotonic Swelling: an Efficient and Safe Route for Cellular Labeling. *Contrast Media Mol. Imaging* **2013**, *8*, 475-486.

(44) Brown, S.; Bailey, D. L.; Willowson, K.; Baldock, C. Investigation of the Relationship between Linear Attenuation Coefficients and CT Hounsfield Units Using Radionuclides for SPECT. *Appl. Radiat. Isot.* **2008**, *66*, 1206-1212.

(45) Best, A. C.; Lynch, A. M.; Bozic, C. M.; Miller, D.; Grunwald, G. K.; Lynch, D. A. Quantitative CT Indexes in Idiopathic Pulmonary Fibrosis: Relationship with Physiologic Impairment. *Radiology*, **2003**, *228*, 407-414.

(46) Isab, A. A.; Hormann, A. L.; Hill, D. T.; Griswold, D. E.; DiMartino, M. J.; Shaw III, C. F. Bis (triethylphosphine) Gold(I) Chloride: Ionization in Aqueous Solution,

Reduction in Vitro of the External and Internal Disulfide Bonds of Bovine Serum Albumin, and Antiarthritic Activity. *Inorg. Chem.* **1989**, *28*, 1321-1326.

(47) Xu, X. Y.; Chong, Y.; Liu, X. Y.; Fu, H.; Yu, C. G.; Huang, J.; Zhang, Z. J. Multifunctional Nanotheranostic Gold Nanocages for Photoacoustic Imaging Guided Radio/Photodynamic/Photothermal Synergistic Therapy. *Acta Biomater.* **2019**, *84*, 328-338.

(48) Alric, C.; Taleb, J.; Le Duc, G.; Mandon, C.; Billotey, C.; Le Meur-Herland, A.; Brochard, T.; Vocanson, F.; Janier, M.; Perriat, P.; Roux, S.; Tillement, O. Gadolinium Chelate Coated Gold Nanoparticles as Contrast Agents for Both X-Ray Computed Tomography and Magnetic Resonance Imaging. *J. Am. Chem. Soc.* **2008**, *130*, 5908-5915.

(49) Roy, I.; Ohulchanskyy, T. Y.; Pudavar, H. E.; Bergey, E. J.; Oseroff, A. R.; Morgan, J.; Dougherty, T. J.; Prasad, P. N. Ceramic-Based Nanoparticles Entrapping Water-Insoluble Photosensitizing Anticancer Drugs: a Novel Dug-Carrier System for Photodynamic Therapy. *J. Am. Chem. Soc.* **2003**, *125*, 7860-7865.

(50) Terreno, E.; Crich, S. G.; Belfiore, S.; Biancone, L.; Cabella, C.; Esposito, G.; Manazza, A. D.; Aime, S. Effect of the Intracellular Localization of a Gd-Based Imaging Probe on the Relaxation Enhancement of Water Protons. *Magn. Reson. Med.* **2006**, *55*, 491-497.

(51) von der Haar, K.; Jonczyk, R.; Lavrentieva, A.; Weyand, B.; Vogt, P.; Jochums, A.; Stah, F.; Scheper, T.; Blume, C. A. Electroporation: a Sustainable and Cell Biology Preserving Cell Labeling Method for Adipogenous Mesenchymal Stem Cells. *Biores.*

Open Access **2019**, *8*, 32-44.

(52) Zhang, Y. H.; Zhang, H. Y.; Li, B. B.; Zhang, H. L.; Tan, B.; Deng, Z. W. Cell-Assembled (Gd-DOTA)$_i$-Triphenylphosphonium (TPP) Nanoclusters as a T_2 Contrast Agent Reveal in Vivo Fates of Stem Cell Transplants. *Nano Res.* **2018**, *11*, 1625-1641.

(53) Srour, N.; Thébaud, B. Mesenchymal Stromal Cells in Animal Bleomycin Pulmonary Fibrosis Models: a Systematic Review. *Stem cells Transl. Med.* **2015**, *4*, 1500-1510.

(54) Chinen, A. B.; Guan, C. M.; Ferrer, J. R.; Barnaby, S. N.; Merkel, T. J.; Mirkin, C. A. Nanoparticle Probes for the Detection of Cancer Biomarkers, Cells, and Tissues by Fluorescence. *Chem. Rev.* **2015**, *115*, 10530-10574

Figure captions

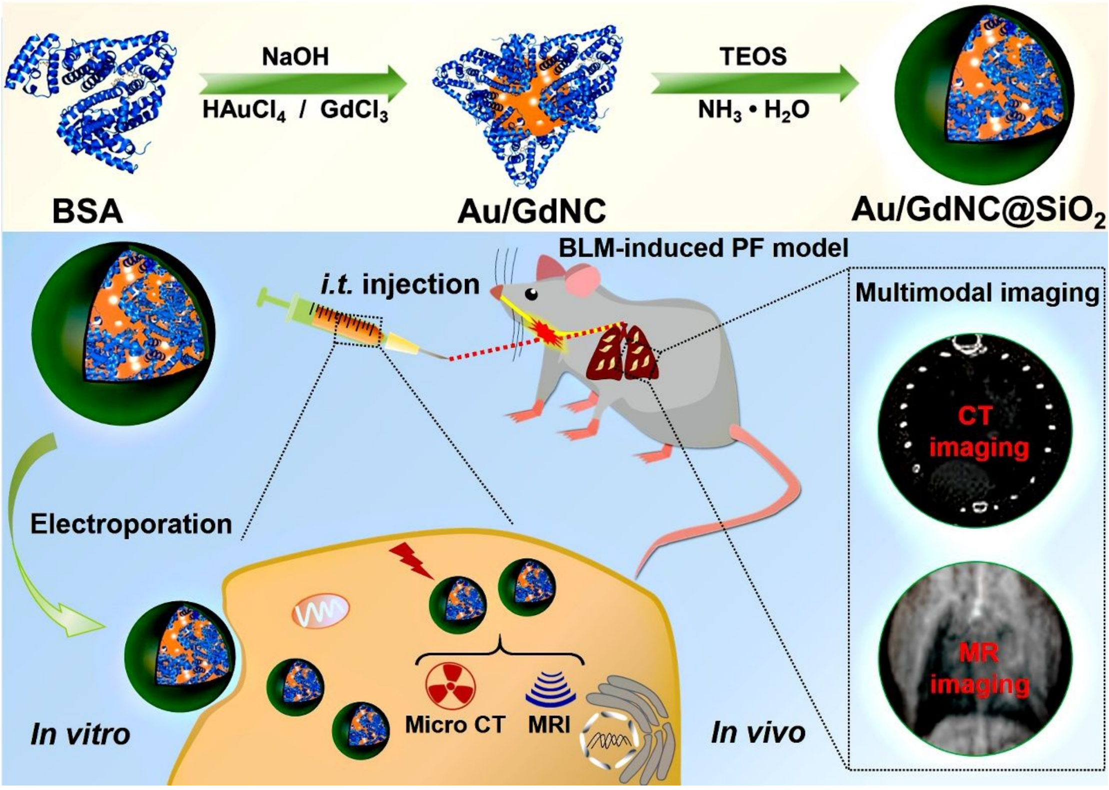

Figure 1. Schematic illustration of the synthesis of Au/GdNC@SiO_2 nanotracer and its application for CT/MR dual-modal imaging tracking of the transplanted hMSCs in a murine model of BLM-induced PF.

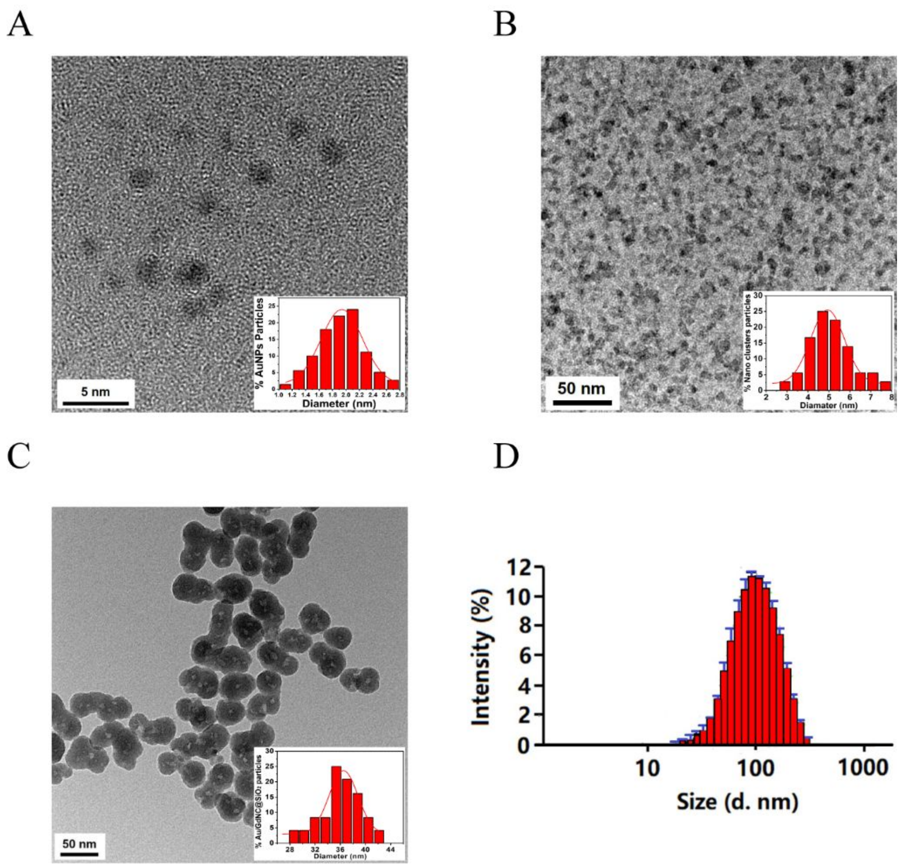

Figure 2. TEM images of (A) AuNC, (B) Au/GdNC, and (C) Au/GdNC@SiO_2. Insets show the size distribution of AuNC, Au/GdNC, and Au/GdNC@SiO_2, respectively. (D) Dynamic light scattering data of Au/GdNC@SiO_2 in aqueous solution.

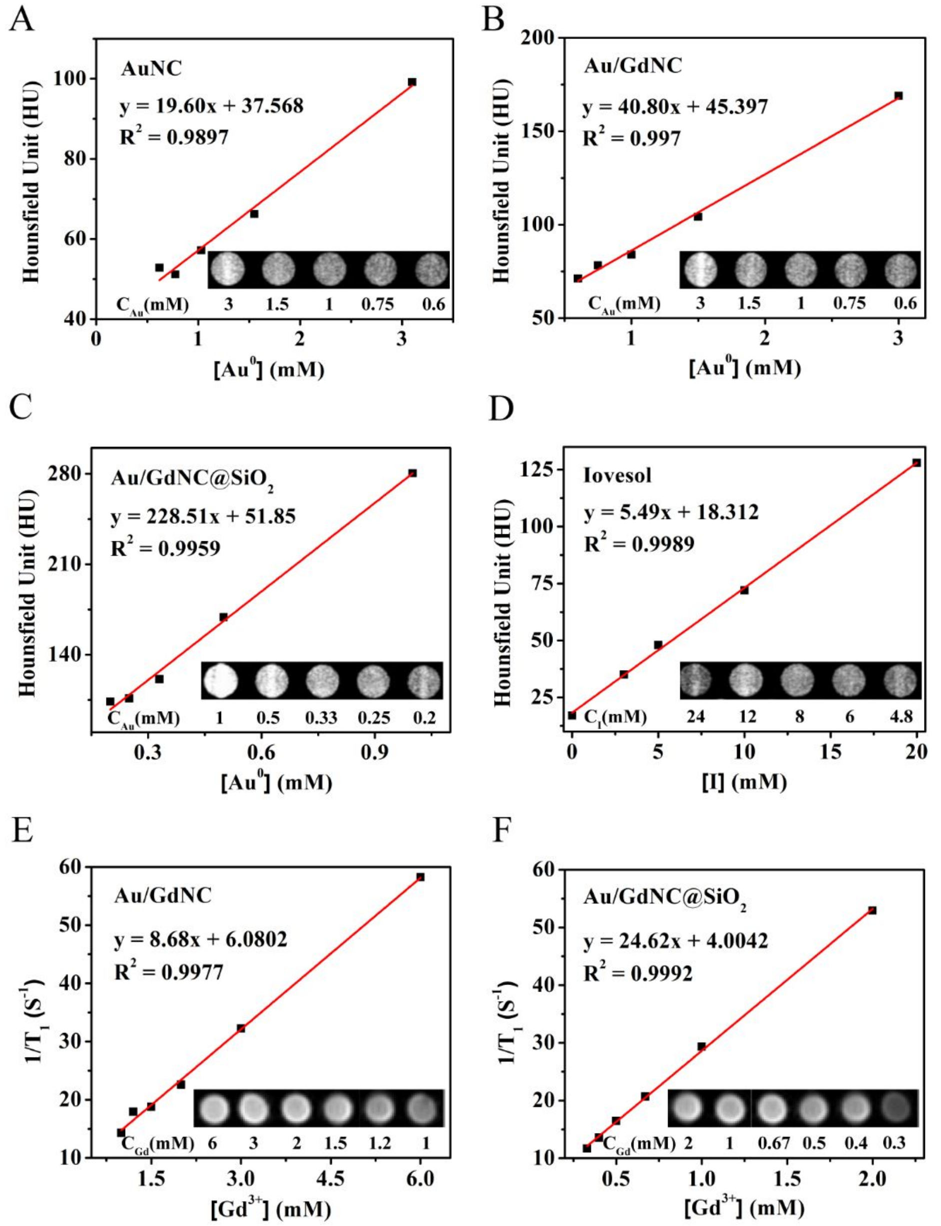

Figure 3. Transverse CT images and plot of calculated HU of (A) AuNC, (B) Au/GdNC, and (C) Au/GdNC@SiO_2 as a function of the Au concentration, respectively. (D) Transverse CT images and calculated HU values of Ioversol as a function of the iodine concentration. And T_1-weighted MR images of (E) Au/GdNC and (F) Au/GdNC@SiO_2 at various Gd concentrations and their relaxivity. The r_1 value was determined from the slope of the plot

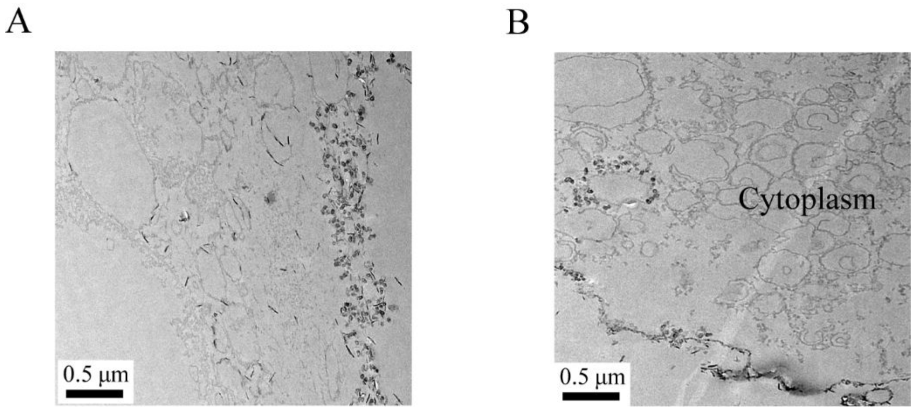

Figure 4. TEM images of the hMSCs EP-labeled with Au/GdNC@SiO_2 (A) immediately, and (B) after 1-day culture and recovery.

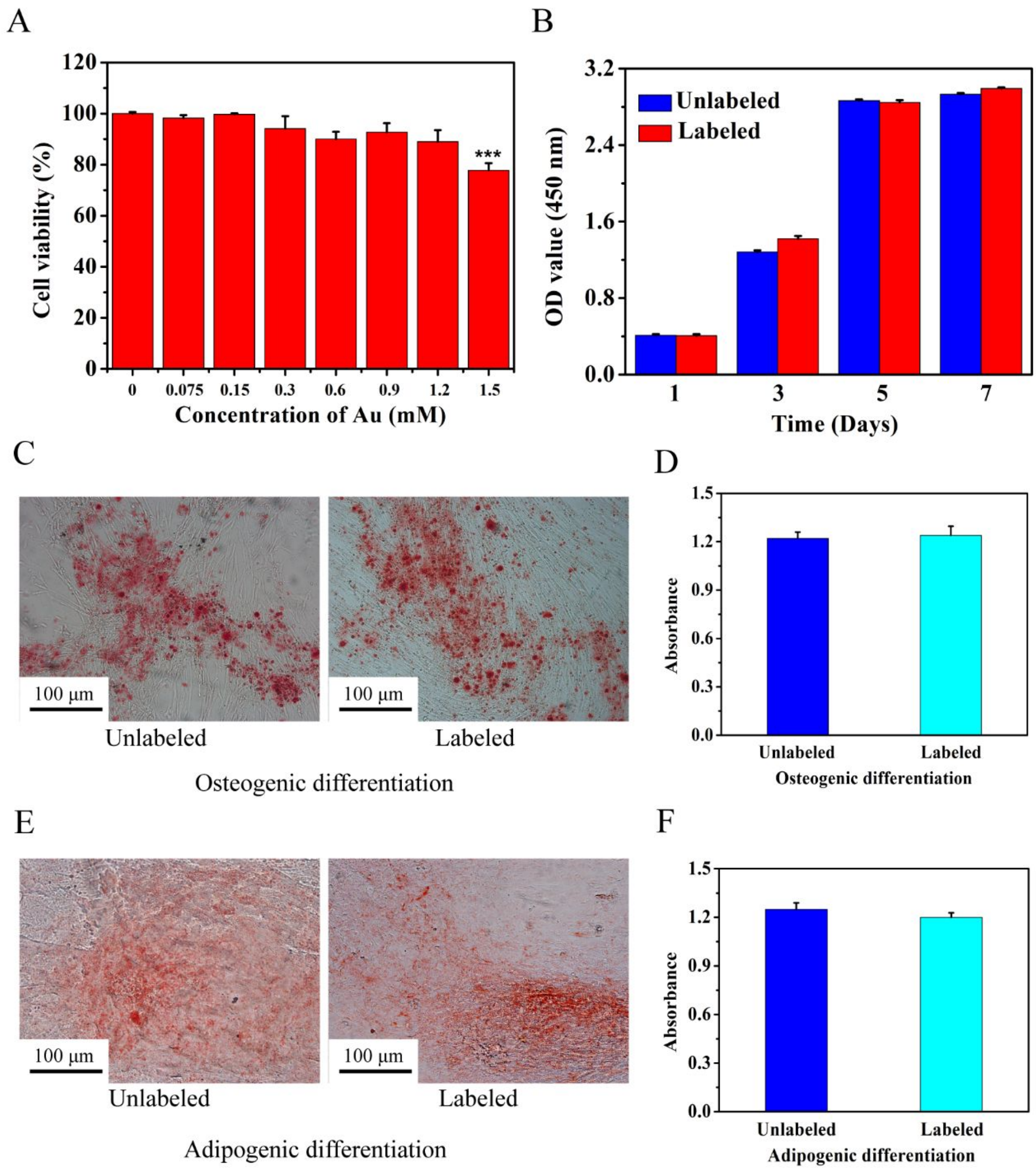

Figure 5. (A) Relative viability of the hMSCs EP-labeled with Au/GdNC@SiO_2 at various Au concentrations after 1-day culture. (B) Proliferation profiles of the hMSCs unlabeled and EP-labeled with Au/GdNC@SiO_2 (1.2 mM of Au). The data were expressed as mean ± standard deviation and the error bars were based on triplicate samples. (C) Alizarin Red S staining and (D) quantification of Alizarin Red S extracted from the osteogenic cells at 550 nm. (E) Oil Red O staining and (F) quantification of Oil Red O extracted from the adipogenic cells at 490 nm.

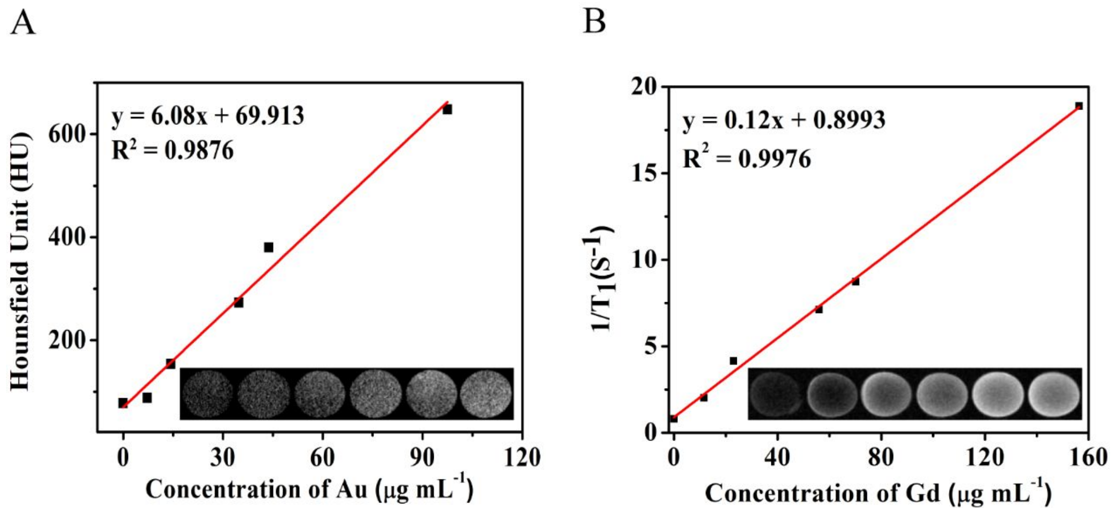

Figure 6. (A) *In vitro* transverse CT images and plot of calculated HU of the hMSCs (2×10^6 cells) EP-labeled with Au/GdNC@SiO_2 as a function of Au concentration. (B) T_1-weighted MR images of the hMSCs (2×10^6 cells) EP-labeled with Au/GdNC@SiO_2 at various Gd concentrations and their T_1 relaxivity.

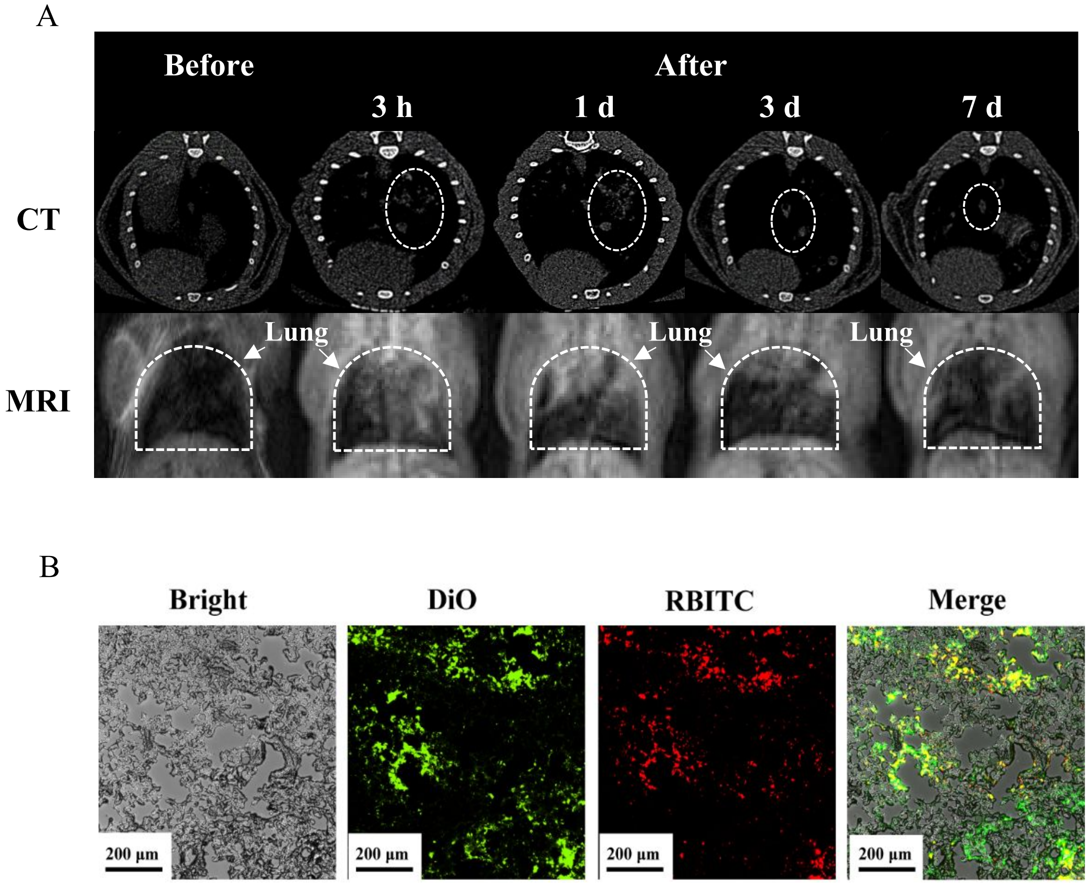

Figure 7. (A) *In vivo* micro-CT and MR images of the Au/GdNC@SiO_2 labeled hMSCs transplanted into the lung of BLM-induced PF mouse after 3 h, 1 d, 3 d and 7 d transplantation, respectively. The images of lung before transplantation were served as the control. The same mouse was observed continuously for 7 days. (B) Fluorescence images of pulmonary frozen sections from the PF mouse sacrificed at the 7d post-transplantation of the labeled hMSCs. The labeled hMSCs were pre-tagged with DiO before RBITC-Au/GdNC@SiO_2 labeling; green fluorescence and red fluorescence refer to DiO-stained cell membrane and RBITC-Au/GdNC@SiO_2, respectively.

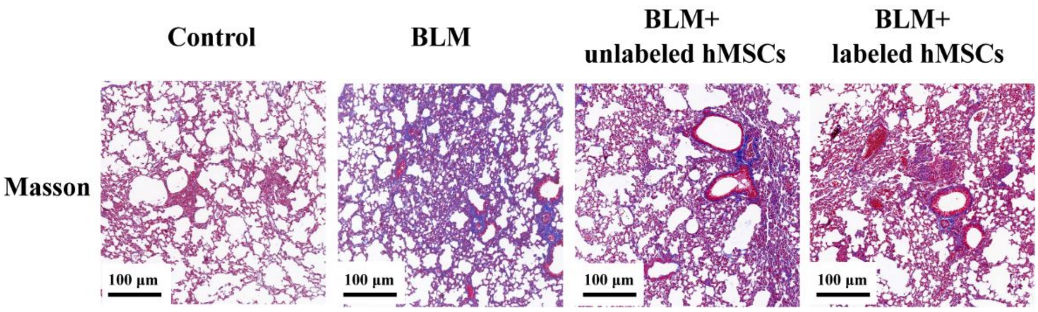

Figure 8. Masson's trichrome staining of the BLM-treated lung sections without and with the unlabeled and the labeled hMSCs transplantation at 7 d post-transplantation. The mice treated with saline were taken as control.

Graphical Abstract